Coronary angiography using laser plasma sources: X-ray source efficiency and optimization of a bent crystal monochromator

Andersson, E; Holzer, G; Forster, E; Gratz, M; Kiernan, L; Sjogren, A; Svanberg, Sune

Published in:
Applied Physics Reviews

DOI:
10.1063/1.1394904

2001

Coronary angiography using laser plasma sources: X-ray source efficiency and optimization of a bent crystal monochromator

E. Andersson, G. Hölzer,[a] and E. Förster[b]
X-Ray Optics Group, Institute of Optics and Quantum Electronics, Friedrich-Schiller-University Jena, Max-Wien-Platz 1, 07743 Jena, Germany

M. Grätz, L. Kiernan, A. Sjögren, and S. Svanberg
Department of Physics, Lund Institute of Technology, P. O. Box 118, S-22100 Lund, Sweden

(Received 25 September 2000; accepted for publication 25 June 2001)

A monochromator has been developed for coronary angiography, comprising a single bent crystal of silicon in Laue transmission geometry. *K* spectra of laser irradiated solid tin and tantalum ($Z=50$ and 73, respectively) targets were measured. The high resolution crystal spectrometer resolve the Sn and Ta $K\alpha$ doublets, allowing in a proof-of-principle experiment the absolute $K\alpha$ photon numbers emitted by the source to be determined. The Ta $K\alpha$ yield is measured as a function of the laser pulse energy, allowing an assessment to be made of the suitability of such sources for medical applications. © *2001 American Institute of Physics.* [DOI: 10.1063/1.1394904]

I. INTRODUCTION

In western countries, about 50% of the cases of death are due to cardiovascular diseases; over 25% of those cases are acute myocardial infarctions. In Germany there are over 200 000 myocardial infarctions per year, 40% of which are fatal. Therefore cardiovascular diseases constitute a most important medical problem. In over 90% of the cases, the reason for a myocardial infarction is a sudden occlusion at a preexistent stenosis in a coronary artery.

Today, the only routinely used method to image the coronary arteries is selective coronary angiography. For this method, a catheter is introduced via the arteries and the aorta into the heart in order to facilitate injection of a contrast agent. However, the method is only performed with strong evidence of heart disease because of the associated morbidity (1.2%–2.2%) and mortality (0.07%–0.23%).[1] The high radiation dose involved in this interventional method using real time x-ray transillumination is also a significant problem which has yet to be solved.

At some synchrotron centers the noninvasive method of dichromography or dual energy subtraction angiography (DESA) has been employed.[2–5] Dichromography after intravenous injection of a contrast agent can reveal minimal contrasts in the image and it is possible to get the contrast image within one heartbeat. However, the cost of a synchrotron prevents its general use for clinical diagnostic imaging. Development of compact sources would be necessary for such diagnostics to be widely utilized.

As Dix[1] reported, great experience was had from the work with patients, 379 since 1990. Because the synchrotron radiation is available in a horizontal plane a special scan chair has been developed, which can move a patient over a distance of 20 cm with a constant speed of up to 50 cm/s. The chair allows a patient rotation of $\pm 180°$ about the vertical axis and $\pm 20°$ about the lateral axis in order to set the appropriate projection angles. The special imaging technique of noninvasive coronary angiography leads to a dose reduction by a factor of 50 because only a relatively small energy band of the whole x-ray spectrum is used. Further dose reduction is due to the short imaging time of 250 ms during one heart beat.

The use of laser produced plasmas as x-ray sources could extend the application of angiography is hospitals. Such a source is nearly point-like with an isotropic radiation characteristic, but due to the short pulse duration (100 fs–5 ps) it emits a relatively small number of photons. Initially, 10 Hz pulse repetition rate lasers have been used.[6] In addition the x-ray optics for energy selection and the detector system must be optimized. The throughput of the crystal, which is used as a monochromator, can be maximized by careful design. Highly sensitive and time-gated[7,8] detectors will help to reduce the image accumulation time, and thereby also the x-ray dose 1 kHz laser systems are now available and have been used for hard x-ray generation with medical applications in mind.[9] The higher repetition rate means that, within a quarter heart beat of 250 ms, one may integrate over a greater shot number. In the current article we present a determination of the absolute photon number from tin and tantalum target materials irradiated by pulses from a 10 Hz high-power laser.

II. THE METHOD

The DESA method (dichromography) is a modification of the *K*-edge subtraction angiography and is based on the abrupt increase of the total attenuation coefficient of a contrast material at *K* edges, cf. Fig. 1.

Each investigation is started with a positioning run with reduced dose. Also the transit time of the contrast agent

[a]Present address: X-Fab Semiconductor Foundries AG, Haarbergstrasse 61, 99097 Erfurt, Germany.
[b]Author to whom correspondence should be addressed; electronic mail: eckhart.foerster@uni-jena.de

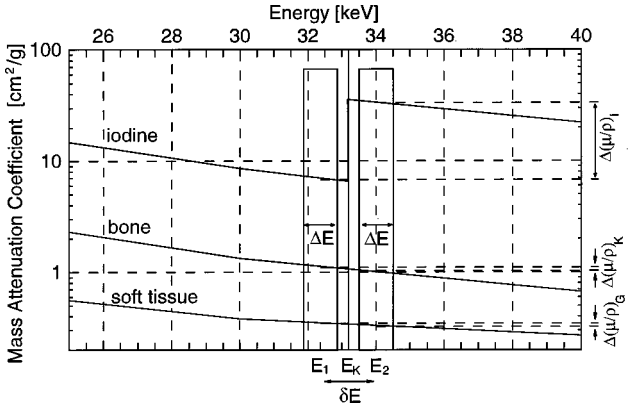

FIG. 1. Energy dependence of the absorption in the region of 25–40 keV around the *K* edge of iodine at 33.17 keV.

through the patient must be measured. The patients chair starts moving only when the contrast agent is distributed in the coronary.

The discontinuity of the absorption at the iodine *K* edge (32.17 keV) is used because it is possible to admit iodine in the form of an organic compound in high concentration to the blood. To a good approximation the energy separation δE of the two mean values E_1 and E_2 of the probing beams (but not their bandwidth ΔE) influences the signal height in the subtracted image, as long as $\Delta E \leqslant \delta E$. That means one image it taken with a nearly monochromatic x-ray energy band below the *K* edge of iodine and the other one with an energy above the *K* edge. By performing a logarithmic subtraction, the subtracted image should contain primarily the iodine image, i.e., the image of the arterial structure. A short selection of suitable target materials for the laser-based DESA method is given in Table I, which also contains data relevant for gadolinium, another medically approved contrast agent. Differential x-ray absorption imaging, which is the principle for DESA, was recently demonstrated in a proof-of-principle study on rats, where a laser-produced plasma source was employed.[10] Primarily, a monochromator-free approach was considered in that paper, but monochromatization increases the contrast.

The high sensitivity of the DESA method, as demonstrated in its prevalent synchrotron radiation implementation, allows an intravenous injection of the contrast agent. The two images are taken at the ''same'' moment when the contrast agent fills the coronary arteries. The use of crystals is necessary for a precise selection of energies around the *K* edge of the contrast agent.

For intravenous injection a complication arises from the fact that not only the coronary arteries, but also the left heart chambers and the aorta are filled simultaneously with the contrast agent. This leads to a superposition of the small arteries on large iodinated structures. To overcome this problem the projection angles must be selected carefully with multiple exposures.

TABLE I. Selection of suitable target materials for angiography with laser produced plasma x-ray sources.

Contrast agent	E_K [keV]	E_1 [keV]	E_2 [keV]
iodine	33.167	33.034 (La $K\alpha_2$)	33.442(La $K\alpha_1$)
		32.194 (Ba $K\alpha_1$)	34.791 (Ce $K\alpha_1$)
gadolinium	50.233	42.996 (Gd $K\alpha_1$)	57.532 (Ta $K\alpha_1$)
		37.361 (Nd $K\alpha_1$)	59.318 (W $K\alpha_1$)

In principle two monochromator geometries, reflection and transmission, can be used for angiography around the iodine and gadolinium *K* edge. At these high energies the Bragg angle of the monochromator crystal is very small, so that the transmission (Laue) geometry is more suitable. Therefore in the next two sections the discussion around the geometrical setup and the intrinsic reflection properties for bent crystals assumes transmission geometry. A detailed description of the reflecting properties in the reflexion or Bragg case can be obtained from Ref. 11.

III. GEOMETRICAL SETUP WITH BENT CRYSTALS

For angiography the size of the field of view (FOV) should be 4×4 in.[2] To realize this FOV one uses the Rowland circle scheme with a bent crystal monochromator in the transmission (Laue) case. The crystal is cylindrically bent with a radius *R* twice the radius of the Rowland circle. A review of the setup in the transmission case including a consistent notation for the geometric parameters can be found in Ref. 12. The geometrical properties can be described by a ''lens'' equation

$$\frac{q_0}{q}+\frac{p_0}{p}=2, \tag{1}$$

where p is the source distance to the crystal and q is the distance to the polychromatic focus, cf. Fig. 2. p_0 and q_0 are the focal distances for monochromatic imaging, if the source is on the Rowland circle, i.e., then $p_0=p$ and $q_0=q$. They can be calculated with the parameters of the bent crystal (bending radius *R*, Bragg angle θ_B, and asymmetry angle ϵ) only.

$$p_0=R\ \cos(\theta_B+\varepsilon) \tag{2}$$

and

$$q_0=R|\cos(\theta_B-\varepsilon)|. \tag{3}$$

We used the same crystal both for the angiography simulation and spectroscopy. Thereby only the direction of curvature must be considered. The radius *R* is defined as positive if the source is on the concave side of the crystal. This constellation is used for angiography in the so-called DuMond geometry, of Fig. 2(a). At any rate p is positive for a real source and q is also positive when on the same side of the crystal.

For angiography we need a divergent x-ray beam and therefore a source distance p with $p_0>p>\frac{1}{2}p_0$. With the distance $q>q_0$, i.e., the distance to the polychromatic focus, and the effective crystal length L_{eff} one finds the distance q_d from the crystal to the detector for a given FOV.

In the case of spectroscopy the crystal is used in the so-called Cauchois geometry, i.e., the source is on the convex side of the crystal. The position of the detector was selected primarily to avoid the position of the polychromatic focus S' because the spectral window is zero at this focus.

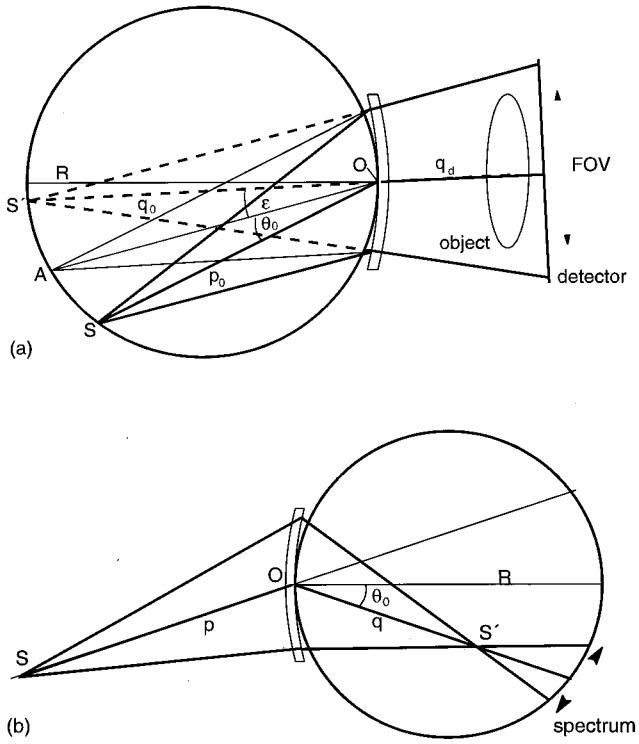

FIG. 2. Scheme of the x-ray optical system in transmission geometry. (a) DuMond geometry for an angiography setup with the source on the Rowland circle and $R>0$, and (b) Cauchois geometry for a spectroscopy setup with the source outside the Rowland circle and $R<0$. *A* is the cross section point of the lattice planes and q_d is the crystal-detector distance.

The best position for the detector is on the Rowland circle, as shown in Fig. 2(b). A shift away from this position leads to a blurred spectrum.

IV. REFLECTION PROPERTIES OF BENT CRYSTALS

The reflection properties depend in a complex way on the choice of lattice planes, the wavelength, the crystal susceptibility, and on the deformation of the crystal lattice (see, for example, Refs. 11, 13, and 14 for bent crystals). Silicon and germanium are the most suitable crystals for high-resolution applications due to their good real structure and elastic properties. The crystal susceptibility and accordingly the strength of reflection are mainly determined by the structure factors F_{hkl} which are given in Table II for the most intense reflections of silicon and germanium. Reflection curves for perfect crystals can be calculated by using the dynamical theory of x-ray diffraction.[15,16] These curves are characterized usually by their peak reflectivity R_{peak}, full width at half maximum (FWHM), and integrated reflectivity R_{int}, i.e., the area under the reflection curve. The curves can be modified considerably by bending the crystal. The reflection curve broadens for decreasing bending radii R,[15,16] cf. Fig. 3.

TABLE II. Reflection parameters for the most intense reflections of silicon and germanium at an energy of 32.54 keV below the *K* absorption edge of iodine.

	Si (Z=14)		Ge (Z=32)	
hkl	θ_B [deg]	F_{hkl}	θ_B [deg]	F_{hkl}
111	3.48	58.1	3.34	151.5
220	5.69	67.3	5.47	178.0
400	8.07	56.6	7.74	142.2

The integrated reflectivity R_{int} increases from the lower dynamical limit (flat crystal) to the upper kinematical limit (mosaic crystal) in fortunate cases. A knowledge of R_{int} is essential for an optimization of the setup and ultimately a quantitative characterization of the source emission. Figure 4 shows higher integrated reflectivity for silicon than for germanium in the range from 20 to 40 keV, where the higher absorption coefficients of germanium outweigh the factor-of-3 difference in structure factors given in Table II. Measurements of the reflection curves are rarely done in the Laue case[13,17] and the results are only relevant if the conditions of the measurement reproduce the real experimental conditions as precisely as possible. To overcome these difficulties, the computer code DIXI[18] has been developed to calculate the intrinsic reflection properties of flat and bent crystals using the dynamical theory of x-ray diffraction in slightly distorted crystals.[19,14] Thus a calibration of the intrinsic reflection properties of bent crystals is possible for any experimental condition and thus the experimental setup can be optimized. The influence of some experimental parameters (crystal material, wavelengths λ, and bending radius R) was already discussed in some detail elsewhere and a bent crystal spectrometer was presented to measure high-resolution Ta $K\alpha$ spectra from a femtosecond laser plasma source.[11]

Although an asymmetric Bragg diffraction geometry is more complicated, it also gives an additional degree of freedom for the experimental setup. The integrated reflectivity, i.e., the throughput of a crystal, can be increased by using an asymmetrically cut crystal with a small curvature radius. Figure 5 shows the integrated reflectivity as a function of the curvature radius R and the asymmetry angle ϵ. The simulations were made for a 0.5 mm thick silicon crystal in asymmetrical reflection 111 at an energy $E=32$ keV. The effect of both factors on the integrated reflectivity can be considerable. The dynamical limit for a flat crystal is $R_{\text{int}}=6.1$ μrad. For an asymmetry of $\varepsilon=35°$ it grows by more than a factor of 40 for a curvature radius of $R=0.7$ m.

Because in the geometry of Fig. 2(a) the crystal touches the Rowland circle only in a single (central) point *O*, it is easy to see that the angle of incidence $\theta=\theta_B+\varepsilon$ must vary slightly over the crystal surface. Only the middle ray hits the crystal lattice planes at the exact Bragg angle. The deviation from this exact angle θ_B is presented in Fig. 6 for different curvature radii in DuMond geometry. This angular error is the maximum angular window which can be reflected by the crystal. If the detuning is larger than the width of reflection curve the effective crystal range will be smaller, i.e., for Bragg diffraction not the whole crystal is used.

The width of the reflection curve (FWHM) limits the size of the crystal which is able to reflect the wavelength λ_0 corresponding to the Bragg angle θ_B. It means that the detuning of the Bragg angle must be smaller than the width of the reflection curve. This is fulfilled as shown in Fig. 6 where also the half-width of the reflection curve (FWHM) is given.

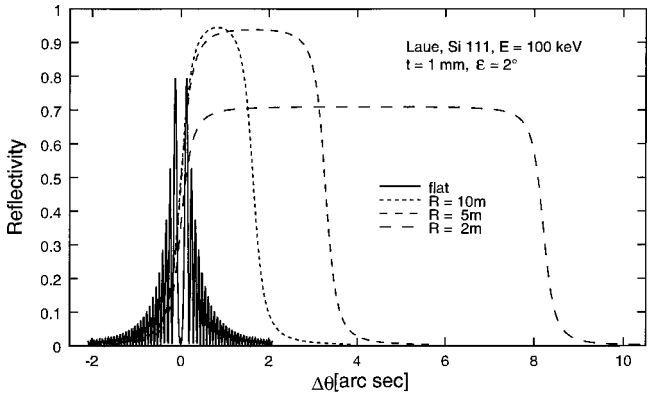

FIG. 3. Typical x-ray reflection curves of flat and cylindrically bent crystals (curvature radius R) in Laue geometry. Energy and asymmetry angle are chosen arbitrarily to show the principal dependence on curvature radius.

V. DETERMINATION OF $K\alpha$ YIELD FROM FS LASER-PRODUCED PLASMAS

A. Laser system and x-ray generation

Studies of the yield from a laser-produced plasma were performed at the Lund Laser Center. The high-power laser system at Lund is based on chirped-pulse amplification in Ti:sapphire. It delivered pulses at about 800 nm with a repetition rate of 10 Hz. Seed laser pulses from a mode-locked oscillator (pulse duration 100 fs) were temporally stretched (2500×) in an all-reflective grating-stretcher arrangement. In a first step, the stretched pulses were amplified in a regenerative amplifier up to a level of 9 mJ. After beam expansion, the pulses were further amplified to 400 mJ in a multipass amplifier. A beam splitter delivered pulses of 100 mJ, which were passed through a spatial filter in order to smoothen the beam profile. The spatially smoothened pulses were amplified up to the 1 J level in a second multipass amplifier. The beam was then further expanded to a diameter of about 50 mm before the pulses were temporally recompressed in a grating compressor. Pulse compression and subsequent beam guiding were done in vacuum in order to avoid pulse distortion due to nonlinear effects.

The recompressed pulses had a duration of 110 fs, as measured by second-order autocorrelation and a focal size of ca. 15 μm, determined with pinhole measurements. Each laser pulse was preceded by two weak prepulses, about 12 and 2 ns before the main pulse. They were of the order of 10^5 and 10^3 times weaker than the main pulse, respectively.

The laser pulses were directed into a target chamber and focused onto a rotating metallic target by means of a diamond-turned, gold-coated parabolic mirror. The pulses were incident at an angle of 30° with respect to the target surface normal. Intensities of 5×10^{17} W cm^{-2} are reached in the focal region, which corresponds to the focal size. A hot

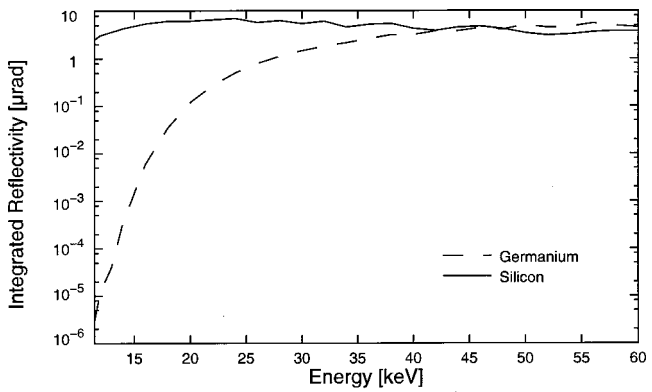

FIG. 4. Integrated reflectivity in the Laue case as a function of energy for silicon and germanium in reflection 111 for a crystal thickness of 0.5 mm.

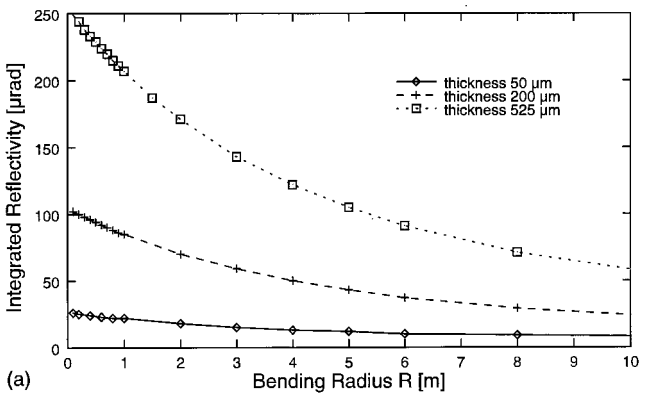

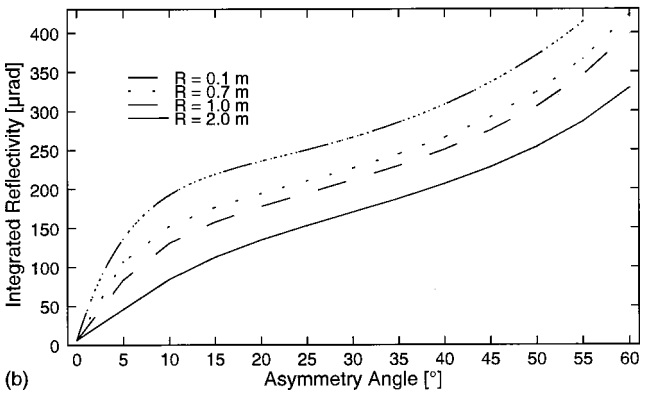

FIG. 5. Integrated reflectivity as a function of curvature radius R (a) and asymmetry angle ε (b).

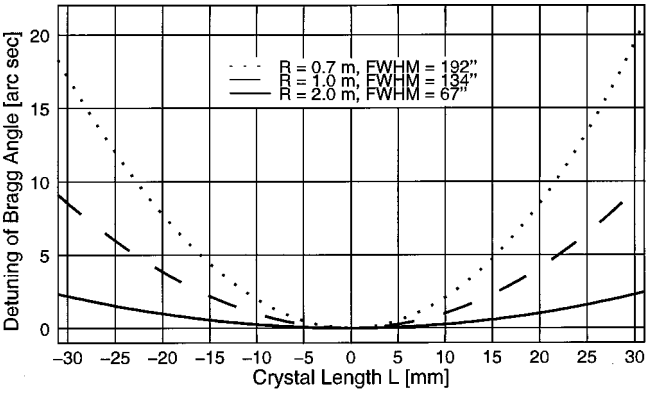

FIG. 6. The difference $\Delta\theta$ between the angle of incidence and the exact Bragg angle as a function of the position on the crystal surface. Calculations were made for a silicon crystal in reflection 111 and an asymmetry angle $\varepsilon=35°$ at an energy $E=32$ keV. The source is on the Rowland circle.

plasma is generated and extremely bright, and ultrashort x-ray pulses are emitted. Solid plates (thickness 3 mm) of tantalum and tin were used as target material.

B. X-ray detection and calibration

A scintillator, coupled to an image-intensified charge coupled device (CCD) camera, was used as the imaging system. A 5 mm thick terbium-doped fiber-optical scintillating plate, coated with aluminum at the x-ray entrance side, was employed (LKH-6, Collimated Holes Inc.,). The use of a scintillating medium in the form of fiber-optical plates results in good spatial resolution, even for a thick scintillator. The fiber-optical plate was placed directly against the image intensifier coupled to a CCD camera (Flamestar IIf, LaVision, Germany). This camera system had a fiber-optical taper connecting the output of the image intensifier to the CCD camera. The effective pixel size in this system was $36\times36\ \mu m^2$. The dynamical range was about 10^4:1.

The scintillator-CCD camera detection system was calibrated with the help of reference radionuclide samples of ^{241}Am, ^{57}Co, ^{133}Ba, ^{137}Cs, ^{54}Mn, ^{60}Co, and ^{22}Na. The samples were placed at a distance of 90 mm from the scintillator. The photon energies and intensities of the different decay paths were obtained from the Table of Isotopes Online Database.[20] Using this procedure, a photon-energy-dependent conversion factor was determined, which related the number of counts in the CCD camera image to the number of absorbed x-ray photons. In the range of 10 keV to 80 keV, the CCD signal is approximately proportional to the energy of the incident photon. The CCD response flattens at higher energies, due to decreasing absorption in the scintillator. The error in this part of the calibration procedure is about 20%.

C. Crystal spectrometer setup

The general setup and the construction of the crystal spectrometer was already described.[11] An adjustable bending device for a triangularly shaped crystal[11,21] was used to achieve a cylindrical curvature of the crystal. The accuracy of the bending radius R was checked by optical and x-ray methods. For spectroscopy in the Laue case a triangular silicon crystal (length 100 mm, base height 35 mm, thickness 1 mm) was manufactured. It is cut asymmetrically to use the reflection 111 with an asymmetry angle $\varepsilon=15°$ in the Cauchois geometry, cf. Fig. 7. A compilation of important experimental setup parameters for Ta $K\alpha$ and Sn $K\alpha$ radiation is shown in Table III.

The source–crystal distance was fixed to $p=350$ mm. The position of the detector was varied and selected primarily to avoid the position of the polychromatic focus.

D. X-ray spectra and $K\alpha$ yield

From the possible target materials given in Table I, two elements, tin and tantalum, respectively, were chosen to determine the absolute photon number in the $K\alpha$ doublet. $K\alpha$, β emission spectra of tin (cf. Fig. 8) were measured using bent crystal spectrometers. The CCD images of the spectra were registered with 300 laser shots. For analysis they were

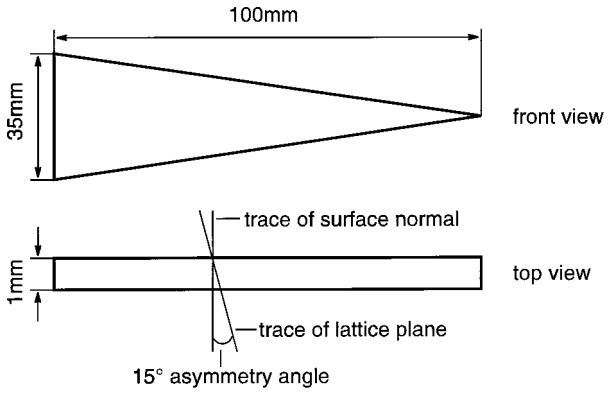

FIG. 7. Schematic drawing of the crystal including the traces of surface normal and reflecting lattice plane.

spatially integrated over a fixed height of 150 pixel, i.e., 5.4 mm. Distances along the dispersion axis were transformed to an energy scale using the peak position of two reference lines, assuming a linear wavelength scale inside the narrow spectral window around the $K\alpha$ (Bragg case) and the $K\alpha,\beta$ lines (Laue case), respectively. Due to the nonlinear transformation from the measured spatial intensity distribution $I(x)$ to the intensity distribution in the energy scale $I_0(E)$ the absolute intensity has to be corrected for the nonlinear line dispersion of the spectrometer according to $I_0(E)=I(x)\frac{dx}{dE}$. The effect of this correction is most significant at the high energy range, i.e., for Bragg angles near zero.

Further correction steps consider the effect of instrument factors. The intensity is recalculated taking into account the wavelength/energy dependence of the integrated reflectivity R_{int}.

The diffracted x-ray photon number of a single crystal can be described by the following integral according to Compton and Allison:[15]

$$N_D=N_S\int_\alpha\int_\phi\int_\lambda G(\alpha,\phi)\cdot j(\lambda)\cdot C\left(\sigma(\alpha,\phi)-\frac{\Delta\lambda}{\lambda}\cdot\tan\,\theta_B\right)d\alpha\,d\phi\,d\lambda. \tag{4}$$

The variables α and ϕ are the horizontal and the vertical divergence angles. G is the angular distribution of the emitted energy and can be set to unity assuming an isotropic emission. j is the photon density distribution in the incidence spectrum, and N_S is the number of photons emitted from the source. The deviation of the Bragg angle is described by the function $\phi=\theta(\alpha,\phi)-\theta_B$.

TABLE III. Experimental parameters for the measurement of the $K\alpha$ emission spectra in the Cauchois geometry (Si crystal, cylindrical curvature $R=-5$ m).

	θ_B [deg]	FWHM [arcsec]	R_{int} [μrad]
Sn $K\alpha_1$	4.5	25.5	80.4
Ta $K\alpha_1$	2.0	24.7	85.2

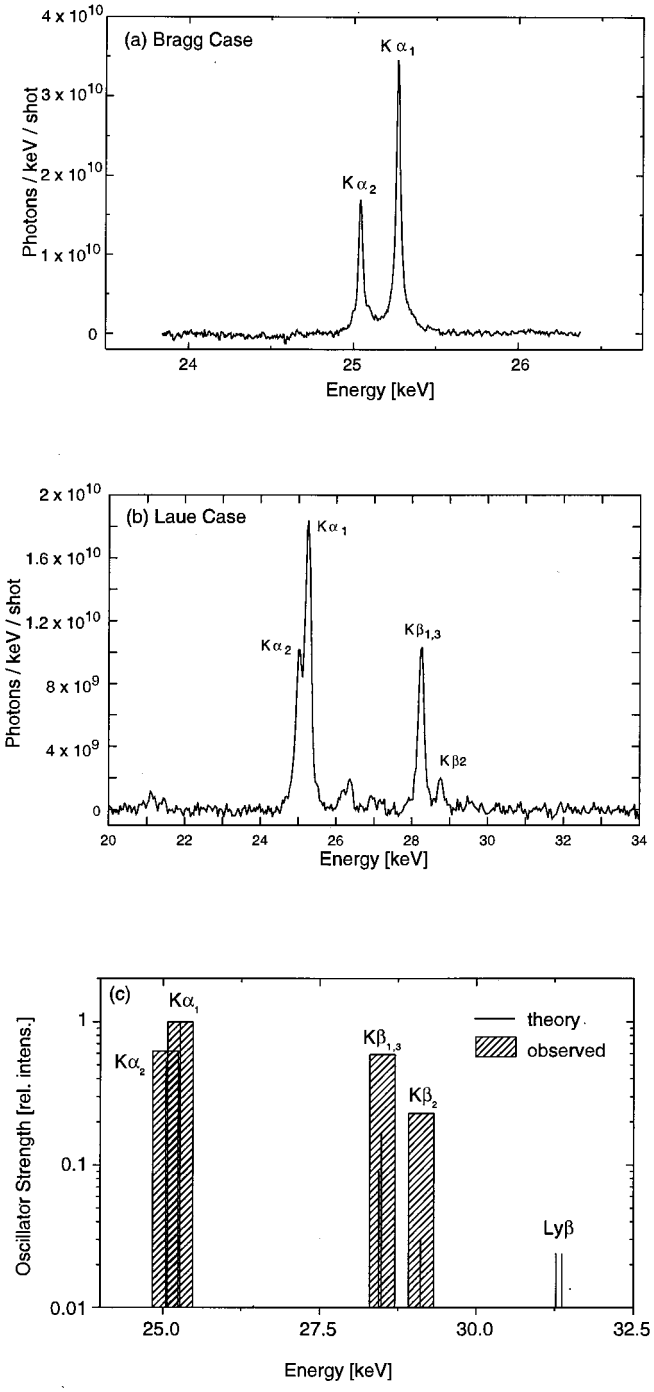

FIG. 8. Absolutely calibrated Sn K spectra, measured (a) in the Bragg (E_L = 950 mJ) and (b) in the Laue geometries (E_L = 750 mJ). (c) shows the comparison of experimental and reference data for the emission line positions and relative line intensities (relative to $K\alpha_1$). Note the well-resolved peak at about 26.3 keV, at the reference position of the Sn L$y\alpha$ doublet.

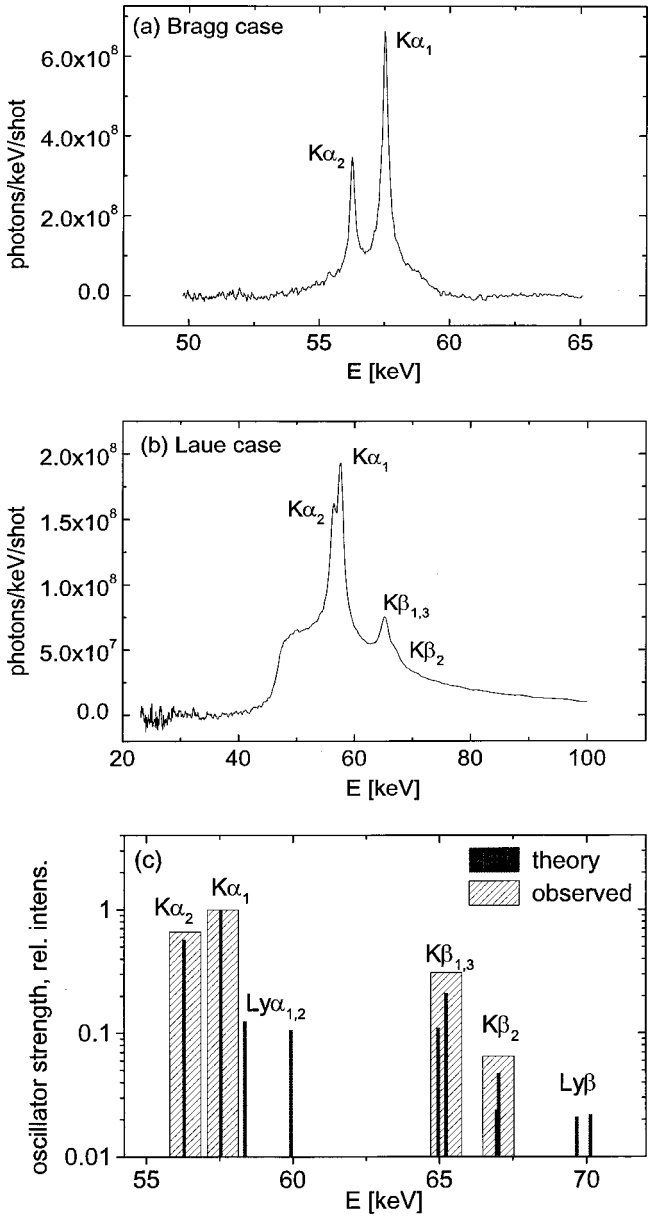

FIG. 9. Absolutely calibrated Ta K spectra, measured (a) in the Bragg (E_L = 950 mJ) and (b) in the Laue geometries (E_L = 750 mJ). (c) shows the comparison of experimental and reference data for the emission line positions and relative line intensities (relative to $K\alpha_1$).

The integral in Eq. (4) can be interpreted as the apparatus function A of the monochromator and is calculated below for special cases. Changing the integration variable λ to θ the apparatus function A is determined by two factors: the integrated reflectivity R_{int} and the geometric factor F_G, i.e., the effective reflecting crystal aperture introduced by the integration limits α and ϕ.

$$A = \frac{N_D}{N_S} = F_G \cdot R_{\text{int}} \quad \text{with} \quad R_{\text{int}} = \int C(\theta - \theta_B)\, d\theta. \tag{5}$$

The apparatus function A must be optimized to be as large as possible.

Finally the photon number per keV per shot from the source is determined using the calibration curve of the detector, the number of laser shots, and the instrument function A of the spectrometer calculated for the reference wavelength (usually $K\alpha_1$). Typical emission spectra of the Sn $K\alpha,\beta$ and Ta $K\alpha,\beta$ series in both geometries are presented in Figs. 8(a) and 8(b) and Figs. 9(a) and 9(b), respectively.

The Sn spectra in the Bragg geometry show the well-resolved $K\alpha$ doublet in a narrow spectral window. In the Laue case the spectral window is broader and additionally

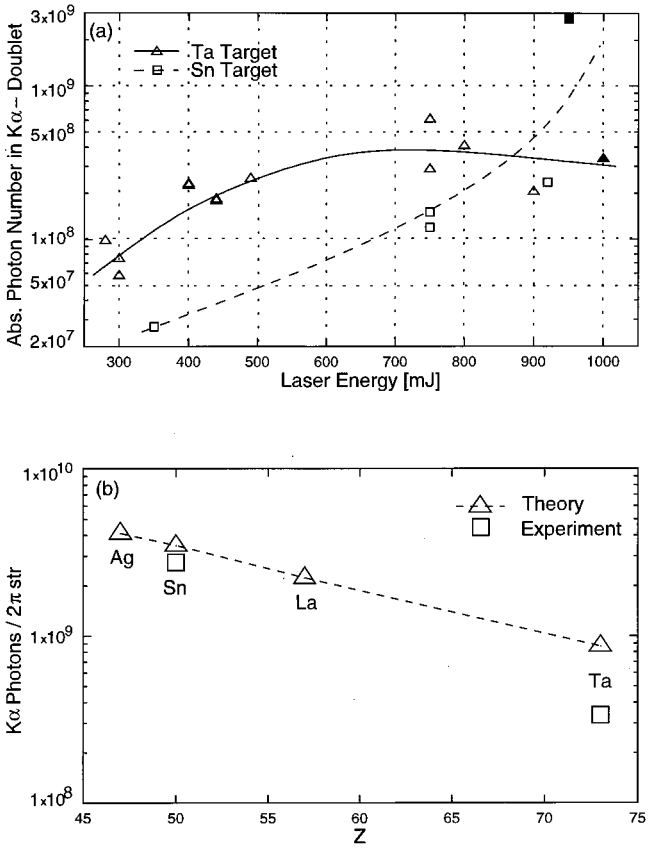

FIG. 10. Comparison of theoretical and experimentally determined $K\alpha$ yield as a function of target material (a) and experimentally determined absolute numbers of photons in $K\alpha$ doublet (b). The curves depict yields calculated using an initial plasma density gradient of $L/\lambda = 1/\lambda[\rho/(d\rho/dz)] = 0.3$. The experimental data in (a) corresponds to the filled points in (b).

the $K\beta$ emission lines are visible. The spectra were fitted to determine the line positions and the integrated line intensities (photon numbers) using an appropriate number of Lorentzians describing the natural line shape. The lines were identified using tabulated positions for the characteristic lines.[22] In Fig. 8(c) the identified lines from experimental spectra in the Laue case are presented and compared to tabulated reference values for the position and the relative intensity (relative to $K\alpha_1$, intensity set to one). The broad bars represent the experimental data, the small ones the reference data.

In the spectra of Sn ($Z=50$) the most intense lines of the K series could be identified: the spectrally resolved $K\alpha$ doublet, the unresolved $K\beta_{1,3}$ doublet, and the unresolved $K\beta_{2,4}$ doublet.[22] Quantitatively, the values of the relative line intensities in the experiment are slightly higher than the tabulated values.[22] This effect, however, is strongly dependent on the precision of the determined background level which was determined only empirically.

For the determination of the $K\alpha$ yield, the Bremsstrahlung background was removed and the spectrum was integrated in the region of the $K\alpha$ doublet. The experimentally determined number of Sn $K\alpha$ and Ta $K\alpha$ photons emitted by the source in 2π srad per laser shot is presented in Fig. 10(a) as a function of the laser energy E_L. Due to the high resolution of the spectra obtained with the crystal spectrometer, a determination of the absolute $K\alpha$ yield is possible, and allows us to compare the experimental results with theoretical calculations,[23] cf. Fig. 10(b). The theoretical points in Fig. 10(b) were determined with combined MC (Monte Carlo) and PIC (particle in cell) calculations using a real laser parameter, i.e., intensity $I=3\times10^{17}$ W cm^{-2}, laser energy before last compression $E_L=1000$ mJ, pulse length $\tau=110$ fs, and focal size $F=30$ μm in full width at half maximum. The $K\alpha$ yield decreases with Z. The experimental points lie just below the $L/\lambda_L=0.3$ curve, which appears to indicate that the plasma conditions were not optimal for $K\alpha$ emission at this laser intensity. At this point further experimental and theoretical studies are necessary.

VI. SETUP FOR ANGIOGRAPHY

To realize a DESA setup the FOV should be illuminated homogeneously with photons. The choice of methods first depends on the shape of the source spectrum.

(1) Use of an x-ray source with predominantely characteristic radiation, e.g., La $K\alpha_1$ or
(2) use of a Bremsstrahlung continuum.

A. A monochromatic x-ray source

For this case we use one $K\alpha$ line with high brightness. The spectral line width is very small compared to the width of the reflection curve, i.e., $\Delta\theta_{\text{line}}=6$ arc sec$\ll\Delta\theta_{\text{cryst}}=200$ arc sec or $\Delta E_{\text{line}}=11.2$ eV$\ll\Delta E_{\text{cryst}}=470$ eV. The optimal geometry is a DuMond geometry with the source at the Rowland circle, cf. Fig. 2. The evaluation of the triple integral of Eq. (4) and simplification leads to

$$A=\frac{N_D}{N_S}=\frac{L_{\text{eff}}\cdot h\cdot\cos(\theta_B+\varepsilon)}{p_0^2}\cdot\frac{1}{4\pi}\cdot R_{\text{peak}}, \tag{6}$$

where L_{eff} is the effective reflecting crystal length, h is the crystal height, θ_B is the Bragg angle, ε is the asymmetry angle of the reflecting lattice planes, and p_0 is the source–crystal distance for a source at the Rowland circle. R_{peak} is the peak reflectivity and represents the maximum of reflection curve.

It should be remembered that (1) the width of the reflection curve $\Delta\theta_{\text{cryst}}$ is larger than the linewidth $\Delta\theta_{\text{line}}$ (see above), and (2) the detuning of the Bragg angle is smaller than the width of the reflection curve. Outside these two conditions, the effective reflected crystal area becomes smaller and not all of the line is used for Bragg diffraction.

As an example, A is 1.5×10^{-4} for a silicon crystal in reflection 111 with an energy $E=25.271$ keV (Sn $K\alpha_1$, below the iodine edge), crystal thickness of 0.525 mm, and a curvature radius of 0.7 m. With the condition that we use x-ray film as a detector, we need 1 photon/μm^2 or 10^{10} photons in an area of 10×10 cm^2 for an optical density of 1. With a 10 Hz Ti:Sa laser which emits 2.76×10^9 photons/shot2π, we need 1.2×10^4 shots. Absorption in the object is not included here but can be compensated for by using a more sensitive detector, i.e., image plate or CCD camera.[24]

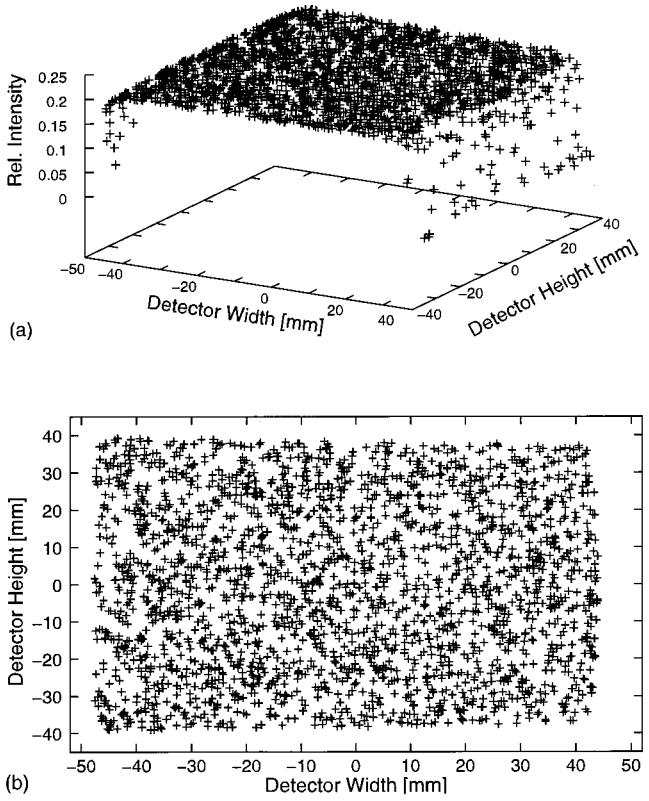

FIG. 11. Intensity distribution in the detector plane. The intensity is normalized to the maximum of the reflection curve.

Figure 11 shows the calculated intensity distribution in the detector plane. The calculations are made with the code LaueRay[25] for a point source at the Rowland circle and an energy of $E=33.442$ keV. The detector distance was fixed to $q_d=500$ mm.

B. A homogeneous continuum as an x-ray source

This technique is analogous to the conditions at a synchrotron source. Here we do not use a special line. From a homogeneous continuum we cut a spectral window by Bragg reflection on the crystal. In this case optimization of luminosity results in an off-Rowland circle position, i.e., the distance to the source can be shorter. The position of the source inside the Rowland circle depends on the spectral window which should be reflected[12]

$$\frac{1}{p}=\frac{\Delta E_{\mathrm{cont}}}{E_{\mathrm{middle}}}\cdot\frac{1}{b\cdot\cot\,\theta_B}+\frac{1}{p_0}, \tag{7}$$

where for transmission geometry $b=L_{\mathrm{eff}}\cdot\cos(\varepsilon+\theta_B)$ is the projection of the effective crystal length on the normal to the incident x rays.

Also, a divergent x ray beam after the crystal limits the source–crystal distance p to $p_0>p>\frac{1}{2}$.

For such an off-Rowland circle position ($K<0.9$ or $K>1.1$), Eq. (4) can be simplified after the integration to

$$A=\frac{N_D}{N_S}=\left|\frac{2K}{K-1}\right|\cdot\frac{h}{p}\cdot\frac{1}{4\pi}\cdot R_{\mathrm{int}}. \tag{8}$$

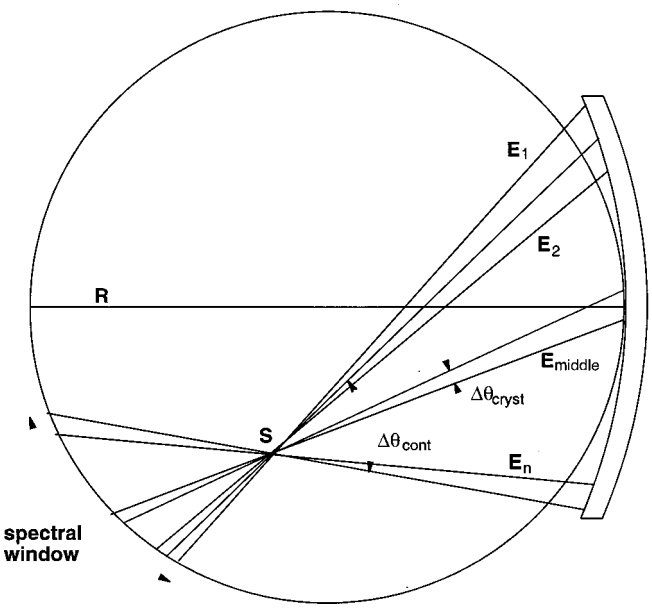

FIG. 12. Scheme of the spectral window ΔE including the different energies E_1 to E_n, which can be reflected by the crystal.

The magnification factor K is defined by the ratio of the polychromatic focus distance q to the source distance p, i.e., $K=q/p$.

As an example A is 1.45×10^{-5} for a silicon crystal in reflection 111 with an energy $E_{\mathrm{middle}}=31$ keV, a spectral window of $\Delta E_{\mathrm{cont}}=1$ keV, a crystal thickness of 0.525 mm, and a curvature radius of 0.7 m.

C. Comparison of both x-ray sources

If we compare both examples it is seen that in the case of using a homogeneous continuum the apparatus function A is at first sight nearly one order of magnitude smaller than with the use of a special characteristic line. However, the calculations are made only with the middle energy $E_{\mathrm{middle}}=1/2(E_1+E_n)$ of the spectral window, cf. Fig. 12. The crystal is able to reflect more than this single energy but this fact is not yet considered in the calculations. The ratio of the spectral window used and the half width of reflection curve is denoted n. For a reflection curve $\Delta\theta_{\mathrm{cryst}}=200$ arc sec ($\Delta E_{\mathrm{cryst}}=470$ eV) and a spectral window of $\Delta E=1$ keV n is about 2. This means that we need a factor of 2 lower photons from the source (1.7×10^{14} photons). Normally the emission in the continuum is a factor of 1000 smaller than in the characteristic line. Thus we need 6×10^7 shots for an optical density of 1. Considering absorption in the object and using a more sensitive detector we get 3×10^7 shots which is inacceptably high.

VII. CONCLUSIONS

Very beneficial both for spectroscopy and for angiography, the integrated reflectivity R_{int} is increased by a factor of 40, i.e., from 6.1 μrad for a flat crystal with symmetrical

reflection to 240 μrad for a bent crystal with $R=0.7$ m, $\varepsilon=35°$, cf. Fig. 5, due to the optimization of the curvature radius and the asymmetry angle.

A thinner crystal, which consequently can be bent to smaller radii, will allow a further optimization of the monochromator setup to a more compact geometry with a shorter source–crystal distance. Potential optimization of the x-ray yield, both in characteristic and continuum, with laser and target parameters has not yet been taken into account. Theoretical and experimental studies are in progress to address this point.[23] For example, enhancing the $K\alpha$ yield with a deliberate prepulse[9,26] and the dependence of a line/continuum ratio on target material and laser intensity.

The exposure time due to the very high number of shots (10^5) will be reduced by using a kHz laser system instead of a 10 Hz laser system with the assumption that the kHz laser system generates the same number of x-ray photons as a 10 Hz laser system per shot. Considerable improvements are required to achieve a fully operational differential absorption imaging system with the additional feature of dose reduction due to time gating.[24]

ACKNOWLEDGMENTS

The authors gratefully acknowledge valuable help from A. Persson, C.-G. Wahlström, O. Wehrhan, I. Uschmann, and J. Tschischgale. The authors also thank W.-R. Dix and W. A. Kaiser for profitable discussion. This work was supported by the European Community (Contract No. FMRX-CT96-0080), the Thuringia Ministry for Science, Research and Arts (Contract-No. B501-96080), the Swedish Natural Science Research Council, the Swedish Medical Research Council, and the Knut and Alice Wallenberg Foundation.

[1] W.-R. Dix, Prog. Biophys. Mol. Biol. **63**, 159 (1995).
[2] G. Illing, J. Heuer, B. Reime, M. Lohmann, R. H. Menk, L. Schildwächter, W.-R. Dix, and W. Graeff, Rev. Sci. Instrum. **66**, 1379 (1995).
[3] C. Schulze, Ph.D thesis, University of Hamburg, 1994.
[4] P. Suortti, W. Thomlinson, D. Chapman, N. Gmür, R. Greene, and N. Lazarz, Nucl. Instrum. Methods Phys. Res. A **297**, 268 (1990).
[5] P. Suortti, W. Thomlinson, D. Chapman, N. Gmür, D. P. Siddons, and C. Schulze, Nucl. Instrum. Methods Phys. Res. A **336**, 304 (1993).
[6] K. Herrlin, G. Svahn, C. Olsson, H. Petterson, C. Tillman, A. Persson, C.-G. Wahlström, and S. Svanberg, Radiology **189**, 65 (1993).
[7] C. L. Gordon III, G. Y. Yin, B. E. Lemoff, P. B. Bell, and C. P. J. Barty, Opt. Lett. **20**, 1056 (1995).
[8] M. Grätz, L. Kiernan, K. Herrlin, C. G. Wahlström, and S. Svanberg, IEEE J. Sel. Top. Quantum Electron. **2**, 1041 (1996).
[9] F. Albert, A. Sjögren, C.-G. Wahlström, S. Svanberg, C. Olsson, and H. Merdji, *Proceedings of X-Ray Lasers*, edited by G. Jamelot, C. Mueller, and A. Klisnick (EDP Sciences, Les Ulis, 2001).
[10] C. Tillman, I. Mercer, S. Svanberg, and K. Herrlin, J. Opt. Soc. Am. **13**, 209 (1996).
[11] G. Hölzer, E. Förster, M. Grätz, C. Tillman, and S. Svanberg, J. X-Ray Sci. Technol. **7**, 50 (1997).
[12] P. Suortti, Rev. Sci. Instrum. **63**, 942 (1992).
[13] P. Suortti and C. Schulze, J. Synchrotron Radiat. **2**, 6 (1995).
[14] P. Penning, Ph.D. thesis, Technical University Delft, 1966.
[15] A. Compton and S. Allison, *X-Rays in Theory and Experiment*, 2nd ed. (van Nostrand, New York, 1957).
[16] Z. G. Pinsker, *Dynamical Scattering of X-Rays in Crystals* (Springer, New York, 1978), p. 59.
[17] C. Schulze and D. Chapman, Rev. Sci. Instrum. **66**, 2220 (1995).
[18] G. Hölzer, O. Wehrhan, and E. Förster, Cryst. Res. Technol. **33**, 555 (1998).
[19] P. Penning and D. Polder, Philips Res. Rep. **16**, 419 (1961).
[20] S. Chu and L. Ekström, Table of Isotopes Online Database (1998). http://nulceardata.nuclear.lu.se/Database/toi/
[21] M. Lemmonier, R. Fourme, F. Rousseaux, and R. Kahn, Nucl. Instrum. Methods **152**, 173 (1978).
[22] G. Zschornack, *Atomdaten für die Röntgenspektralanalyse*, 1. ed. (VEB Deutscher Verlag für Grundstoffindustrie, Leipzig, 1989).
[23] Ch. Reich, P. Gibbon, I. Uschmann, and E. Förster, Phys. Rev. Lett. **84**, 4846 (2000).
[24] M. Grätz, Ph.D. thesis, Lund Institute of Technology, 1998.
[25] J. Tschischgale, LAUERAY: Raytracing program for a transmission spectrometer (unpublished).
[26] S. Bastiani, A. Rousse, J. P. Geindre, P. Audebert, C. Quoix, G. Hamoniaux, A. Antonetti, and J.-C. Gauthier, Phys. Rev. E **56**, 7179 (1997).